Title

Silicon on ultra-low-loss waveguide photonic integration platform

Permalink

https://escholarship.org/uc/item/97b7k0w7

Journal

Optics Express, 21(1)

Authors

Bauters, Jared
Davenport, Michael
Heck, Martijn
et al.

Publication Date

2013-01-07

Silicon on ultra-low-loss waveguide photonic integration platform

Jared F. Bauters,[1,*] Michael L. Davenport,[1] Martijn J. R. Heck,[1] J. K. Doylend,[1] Arnold Chen,[2] Alexander W. Fang,[2] and John E. Bowers[1]

[1]*Department of Electrical and Computer Engineering, University of California, Santa Barbara, CA 93106, USA*
[2]*Aurrion, Inc., 130 Robin Hill Rd. Suite 300, Goleta, CA 93116, USA*
[*]*jbauters@ece.ucsb.edu*

Abstract: We demonstrate a novel integrated silicon and ultra-low-loss Si_3N_4 waveguide platform. Coupling between layers is achieved with (0.4 ± 0.2) dB of loss per transition and a 20 nm 3-dB bandwidth for one tapered coupler design and with (0.8 ± 0.2) dB of loss per transition and a 100 nm 3-dB bandwidth for another. The minimum propagation loss measured in the ultra-low-loss waveguides is 1.2 dB/m in the 1590 nm wavelength regime.

©2013 Optical Society of America

OCIS codes: (130.0130) Integrated optics; (230.7390) Waveguides, planar.

References and links

1. D. T. Spencer, Y. Tang, J. F. Bauters, M. J. R. Heck, and J. E. Bowers, "Integrated Si_3N_4/SiO_2 ultra high q ring resonators," in *Proceedings of IEEE Photonics Conference* (IEEE, 2012) 141–142.
2. F. Vollmer, D. Braun, A. Libchaber, M. Khoshsima, I. Teraoka, and S. Arnold, "Protein detection by optical shift of a resonant microcavity," Appl. Phys. Lett. **80**(21), 4057–4059 (2002).
3. C. Ciminelli, F. Dell'Olio, C. E. Campanella, and M. N. Armenise, "Photonic technologies for angular velocity sensing," Adv. Opt. Photon. **2**(3), 370–404 (2010).
4. K. Horikawa, I. Ogawa, T. Kitoh, and H. Ogawa, "Silica-based integrated planar lightwave true-time-delay network for microwave antenna applications," in *Proceedings of the Optical Fiber Communication Conference* **2**, 100–101 (1996).
5. X. S. Yao and L. Maleki, "Optoelectronic microwave oscillator," J. Opt. Soc. Am. B **13**(8), 1725–1735 (1996).
6. D. Liang and J. E. Bowers, "integrated optoelectronic devices on silicon," in *MRS Proceedings* **1396**, (2012).
7. T. Tsuchizawa, K. Yamada, T. Watanabe, S. Park, H. Nishi, R. Kou, H. Shinojima, and S. Itabashi, "Monolithic integration of silicon-, germanium-, and silica-based optical devices for telecommunications applications," IEEE Journ. of Sel. Top. in Quant. Elec. **17**, 516–525 (2011).
8. L. Agazzi, J. D. B. Bradley, M. Dijkstra, F. Ay, G. Roelkens, R. Baets, K. Wörhoff, and M. Pollnau, "Monolithic integration of erbium-doped amplifiers with silicon-on-insulator waveguides," Opt. Express **18**(26), 27703–27711 (2010).
9. L. Chen, C. R. Doerr, and Y. Chen, "Polarization-Diversified DWDM Receiver on silicon free of polarization-dependent wavelength shift," in *Proceedings of OFC,* (Optical Society of America, 2012), paper OWG3.7.
10. J. F. Bauters, M. J. R. Heck, D. D. John, J. S. Barton, C. M. Bruinink, A. Leinse, R. G. Heideman, D. J. Blumenthal, and J. E. Bowers, "Planar waveguides with less than 0.1 dB/m propagation loss fabricated with wafer bonding," Opt. Express **19**(24), 24090–24101 (2011).
11. A. M. Agarwal, L. Liao, J. S. Foresi, M. R. Black, X. Duan, and L. C. Kimerling, "Low-loss polycrystalline silicon waveguides for silicon photonics," J. Appl. Phys. **80**(11), 6120–6123 (1996).
12. J. F. Bauters, M. J. R. Heck, D. John, D. Dai, M. C. Tien, J. S. Barton, A. Leinse, R. G. Heideman, D. J. Blumenthal, and J. E. Bowers, "Ultra-low-loss high-aspect-ratio Si_3N_4 waveguides," Opt. Express **19**(4), 3163–3174 (2011).
13. J. F. Bauters, M. J. R. Heck, D. Dai, D. D. John, J. S. Barton, D. J. Blumenthal, and J. E. Bowers, "High Extinction, Broadband, and Low Loss Planar Waveguide Polarizers," in *Proceedings of IPR*, (Optical Society of America, 2012), paper ITu2B.2.
14. A. Yariv, *Optical Electronics in Modern Communications Fifth Edition* 526–531 (Oxford University Press, 1997).
15. G. Roelkens, P. Dumon, W. Bogaerts, D. V. Thourhout, and R. Baets, "Efficient silicon-on-insulator fiber coupler fabricated using 248-nm-deep UV lithography," Phot. Tech. Lett. **17**(12), 1–3 (2005).
16. M. G. F. Wilson and G. A. Teh, "Tapered optical directional coupler," IEEE Trans. on Micr. Theory and Tech. **23**(1), 85–92 (1975).
17. D. Dai, Y. Tang, and J. E. Bowers, "Mode conversion in tapered submicron silicon ridge optical waveguides," Opt. Express **20**(12), 13425–13439 (2012).
18. H. Lee, T. Chen, J. Li, O. Painter, and K. J. Vahala, "Ultra-low-loss optical delay line on a silicon chip," Nat. Comm. **3**, 1–7 (2012).

19. J. W. Nicholson, A. D. Yablon, S. Ramachandran, and S. Ghalmi, "Spatially and spectrally resolved imaging of modal content in large-mode-area fibers," Opt. Express **16**(10), 7233–7243 (2008).

1. Introduction

Ultra-low-loss silica-based waveguides (ULLWs) on silicon have propagation losses 100 to 1000 times lower than silicon or III-V based semiconductor waveguides. They also have efficient coupling with optical fibers, reduced sensitivity to perturbations, and have been used as planar ultra-high-Q resonators [1]. This technology has advantages for many applications, including sensors [2], gyroscopes [3], adjustable delay lines for buffers or true time delay phased array radars [4], and low phase noise oscillators [5]. Ultra-low-loss waveguides require high temperature processing of over 1000 °C and have not been integrated with lasers and photodetectors, which are required for fully integrating the abovementioned photonic systems. Lasers, modulators, and photodetectors have been integrated with silicon based devices using heterogeneous integration of III-V epitaxial layers through bonding [6]. However, the ultra-low-loss and silicon waveguides are very different. The ULLWs support a large mode with a low effective index (~1.5), and the silicon waveguides have a smaller mode with a much higher index (~3.4). A process that enables the integration and low loss coupling of ultra-low-loss waveguides with active elements is needed.

Recently, researchers have integrated silicon and silica-based waveguides using a front-end process shown schematically in Fig. 1(a) [7–9]. In this process, the silica-based waveguide's films are deposited on a silicon-on-insulator wafer after the fabrication of silicon waveguides and devices on that wafer. Two characteristics of a front-end process are prohibitive for obtaining silicon photonics integrated with ultra-low-loss waveguides and high-Q resonators. First, a front-end integration process limits the cladding thickness between the silica-based waveguide's cores and the silicon substrate to the sum of the buried oxide (BOx), SOI silicon, and coupling gap thicknesses. Since the two waveguides should couple, the coupling gap thickness cannot be arbitrarily large. For typical SOI BOx thicknesses of 3 μm or less, this limits the silica-based waveguide's lower cladding thickness to less than the 15 μm needed for ultra-low-loss. Second, a front-end process disallows a high temperature anneal of the silica-based waveguide's films. A high temperature anneal is needed for driving impurity hydrogen out from the core and cladding layers to obtain ultra-low loss, but it would degrade the performance of the active devices in a front-end process [7].
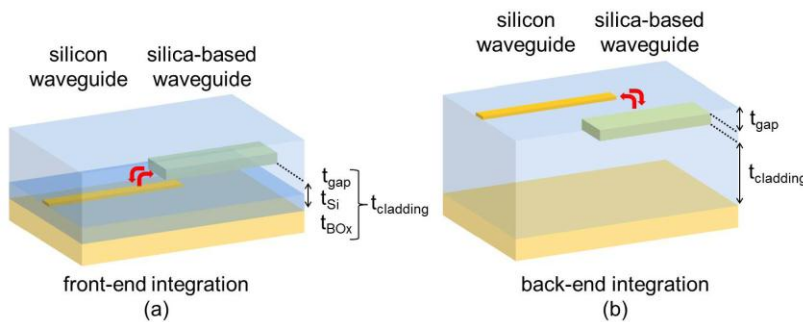

Fig. 1. Schematic views of (a) front-end and (b) back-end schemes for integrating silicon photonics with silica-based waveguides.

In this work, we demonstrate a novel back-end integration process with low coupling loss shown schematically in Fig. 1(b). In this process, the thin Si layer of an SOI die is transferred to the top of an ultra-low-loss waveguide die via oxide-to-oxide bonding, thus avoiding limitations on the thickness of the cladding layer between the silica-based waveguide's cores and the Si substrate. The silica-based waveguides are also annealed at a high temperature (1050 °C) before integration of the silicon layer. These characteristics enable ultra-low propagation loss in the silica-based waveguides integrated with silicon photonics. Moreover, this process is fully compatible with the existing CMOS fabrication infrastructure.

We begin this paper with a description of the back-end integration process (Section 2). We then quantify the small effect this process has on propagation loss in the ultra-low-loss waveguides by comparing waveguides that have and have not undergone integration with silicon photonics (Section 3). Finally, we discuss optical coupling between the Si and ultra-low-loss waveguide layers, which is achieved with a lateral taper of the Si waveguide (Section 4).
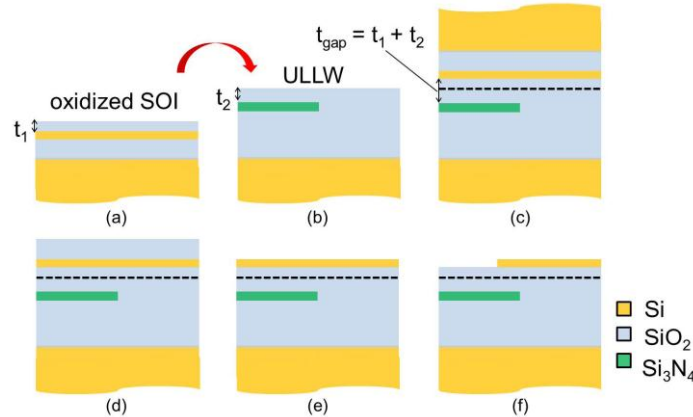
2. Fabrication process

Fig. 2. A schematic overview of the back-end integration process used in this work.

Figure 2 outlines the fabrication process used for integrating silicon photonics with ultra-low-loss waveguides. In this work, the process is performed at the die level, though full wafer processing is possible. Figure 2(a) shows an SOI die with thermal SiO_2 of thickness t_1 grown on top of the thin Si layer. Figure 2(b) shows a fabricated ultra-low-loss waveguide die. In this work, the ULLWs are fabricated on 200 mm Si substrates in a CMOS foundry using 248 nm stepper lithography. Though the ULLW core is Si_3N_4, more than 85% of the TE mode power is in the SiO_2 cladding layers. The lower SiO_2 cladding is 15 μm thick, such that substrate leakage loss is negligible for the fundamental TE mode. The waveguides are annealed at 1050 °C to reduce the impurity hydrogen concentration in the deposited films, enabling ultra-low propagation loss. More details on the ULLWs can be found in Section 3 of this paper as well as in [10]. In Fig. 2(c), the oxidized SOI die is bonded to the planarized ULLW die using an O_2 plasma assisted process [10]. The strength of the bond is then increased with a 3 hour anneal in a nitrogen environment at 950 °C. After bonding, the optical coupling gap thickness (t_{gap}) is the sum of the ULLW wafer's upper cladding thickness (t_2 in the figure) and the thickness of SiO_2 thermally grown on the SOI wafer (t_1).

In Fig. 2(d), the SOI die's silicon substrate is removed. Most of the Si is removed in an initial mechanical lapping and polishing step. The final ~100 μm is removed in a dry etch that is selective to the BOx layer underneath. In Fig. 2(e), the BOx layer is removed using buffered hydrofluoric acid, which is selective to the thin Si layer of the SOI wafer. Figure 3(a) shows a scanning electron microscope image of a die at this step in the process. Unlike with Si deposition techniques [11], smooth crystalline Si makes up the top layer of the bonded die, and the Si thickness tolerance of the original SOI wafer is preserved – a key advantage to this approach. An RMS roughness of 0.49 nm is measured at the surface of the thin Si layer using an atomic force microscope (see Fig. 3(a)). This surface roughness is low enough for additional bonding of III-V epitaxial layers. In Fig. 2(f), a dry etch defines the Si waveguides. Figure 3(b) shows a top-down microscope picture of a die after Si waveguide processing. The Si s-bend and spiral structures are coupled to straight ULLWs underneath. Standard hybrid silicon processing can then be used to bond III-V gain and absorption materials for lasers and photodetectors. This process and the device performance are described in detail in [6].
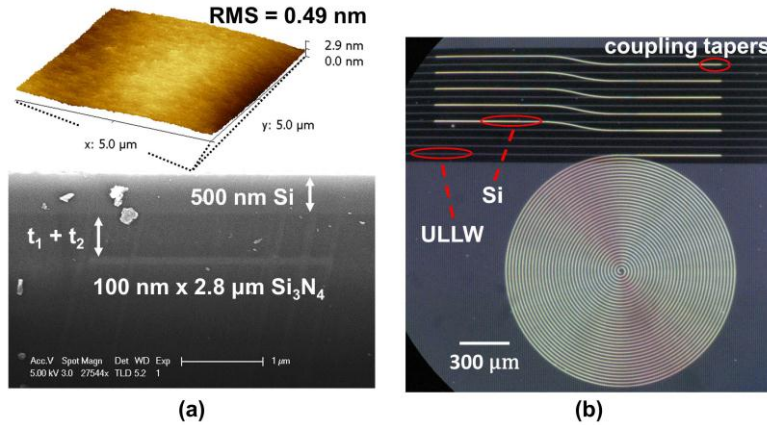
Fig. 3. (a) A scanning electron microscope image of an ULLW with a 500 nm silicon layer bonded on top. Atomic force microscope (AFM) data measured at the Si surface are shown above. (b) A top-down microscope image of Si waveguides coupled to ULLWs below. The Si spiral is 78 mm long.

3. Ultra-low-loss waveguides with and without integration
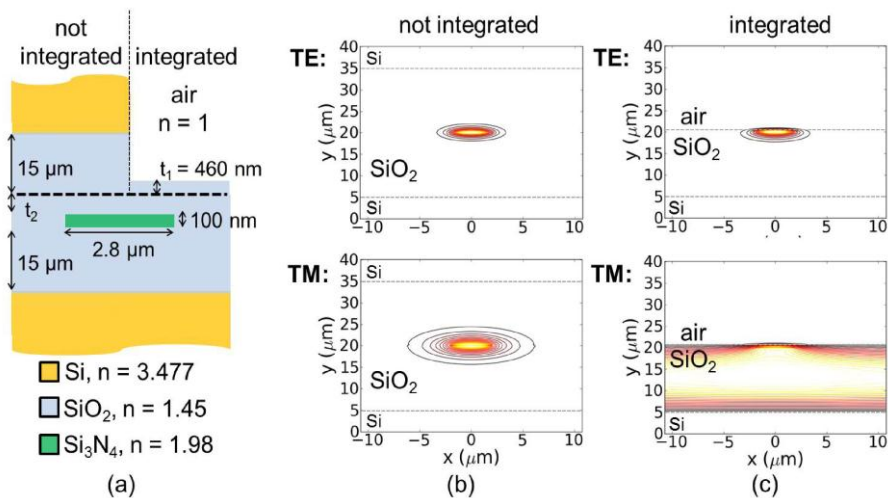
3.1 Waveguide cross section and mode fields

Fig. 4. (a) A schematic cross section of an ULLW with and without integration, and the simulated TE (E_x) and TM (E_y) mode fields for ULLWs (b) without and (c) with Si photonics integrated. Simulations are performed with Photon Design's FIMMWAVE at $\lambda_0 = 1.55$ μm.

Figure 4(a) shows a cross section of the ULL Si_3N_4 waveguides used in this work. The upper part of the cross section is divided to point out the structural differences between these silica-based waveguides with and without integrated silicon photonics. We consider integrated ULL waveguides in a region with no Si waveguide above (see the section labeled "ULLW" in Fig. 3(b)). Where ULLWs without integration have 15 μm of additional bonded thermal SiO_2 upper cladding [10], waveguides with integration have a thinner 460 nm layer (t_2). The thickness of this SiO_2 layer comes from thermally oxidizing 200 nm of Si on the SOI wafer before bonding, reducing the Si waveguide layer's thickness to 500 nm from the 700 nm starting thickness. The bottom half of Fig. 4(a) shows the Si_3N_4 core, which has a high aspect

ratio to reduce sidewall scattering loss [12]. The upper cladding, t_2, of the ULL waveguide is ~150 nm, while the lower thermal SiO_2 cladding is 15 μm thick.

Figs. 4(b) and (c) show simulated mode fields for ULL waveguides with and without integrated silicon photonics, respectively. Though a large birefringence is observed from the difference between the TE and TM mode areas for waveguides without integration in Fig. 4(b), the waveguides support guided TE and TM modes. Figure 4(c) shows the effects that a thinner, 600 nm ($t_1 + t_2$) upper cladding has on the TE and TM mode fields. The TE mode becomes asymmetric about the horizontal axis since the electric field moves away from the air above and further into the lower SiO_2 cladding. The effect on the TM mode is more dramatic, as the guided TM mode is cut-off such that only a cladding mode exists in the films. The TM cladding mode diffracts in the lateral direction and leaks into the Si substrate below. In [13], we showed that the combination of these optical losses for the TM mode can be as high as 25 dB/cm in a straight waveguide. So the integration approach turns a highly birefringent waveguide into a single-polarization or truly single-mode waveguide. Polarization rotators are then necessary at the chip input for applications requiring an interface to optical fiber, which output light in an arbitrary polarization state. However, many applications benefit from the single-polarization property of the ULLW [13], most notably applications that make use of on-chip optical sources and amplifiers.

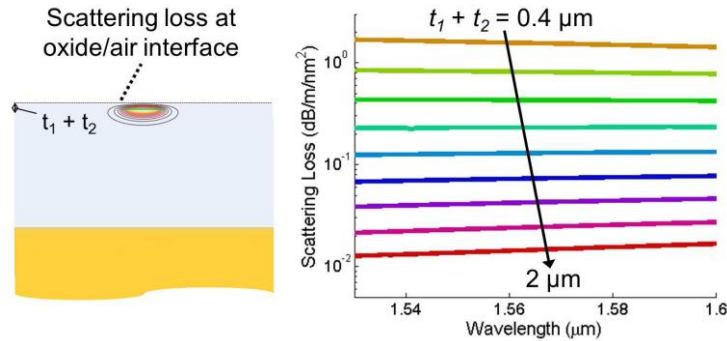*3.2 TE propagation loss in the silica-based waveguides with Si_3N_4 cores*

Fig. 5. Simulated TE scattering loss versus wavelength at the SiO_2/air interface. A 2.8 μm wide core is simulated. The simulated roughness is 1 nm RMS with a correlation length of 50 nm.

Though the TE mode is guided with the thinner 600 nm upper cladding of the integrated structure, the proximity of the air/silica interface gives additional scattering loss. In Fig. 5, we use the three dimensional equivalent current source model discussed in [12] to determine if the added scattering loss is significant. The simulated values in Fig. 5 are for an RMS roughness of 1 nm, and a correlation length of 50 nm is used to model the spectral distribution of the roughness. The figure shows that the scattering loss decreases with increasing thickness of the upper cladding ($t_1 + t_2$) since the field at the interface decreases exponentially as this interface moves away from the core. For thinner upper claddings, the loss decreases with increasing wavelength, as is typically observed for scattering losses. For thicker upper claddings, a regime where scattering loss increases with increasing wavelength exists. This occurs because of the decrease in core confinement (or the increase in field amplitude at the interface) with increasing wavelength. For the upper cladding thickness of 600 nm and an RMS roughness of 0.25 nm measured via AFM in this work, an additional loss of ~0.05 dB/m is simulated. So the integration process must leave a smooth SiO_2/air interface with a roughness smaller than 1 nm to avoid a 1 dB/m contribution to the total propagation loss, which would be on the order of the total loss of the ULLWs, as described below. This loss can also be mitigated by increasing the upper cladding thickness, but the thickness cannot be arbitrarily large since the silicon and ULL waveguides must be in close enough proximity for efficient optical coupling to occur.

Figure 6(a) compares the measured propagation loss versus wavelength for waveguides with 600 nm (the structure with integration) and 15 μm (the structure without integration) upper claddings. The propagation loss is measured from a fit to waveguide optical backscatter as described in [10]. The waveguide backscatter is measured in a 1 m long spiral with maximum and minimum bend radii of 7.2 and 1.7 mm, respectively. Each waveguide has a Si_3N_4 core that is 100 nm thick. In each waveguide, loss increases near $\lambda_0 = 1520$ nm where an N-H bond resonance causes additional loss. The propagation losses differ by at most 20% across the measured spectrum, and the loss in the waveguide with thinner 600 nm upper cladding is actually lower near $\lambda_0 = 1600$ nm. This indicates that the propagation loss in the integrated structure can be as low as that observed in waveguides without integrated silicon photonics. Figure 6(b) shows how tapering the waveguide core to a width of 6 μm can decrease the propagation loss to a minimum of 1.2 dB/m in the $\lambda_0 = 1590$ nm regime. A linear taper from a single-mode 2.8 μm core width at the ULL waveguide input is used to excite the fundamental mode of the 6 μm wide core.
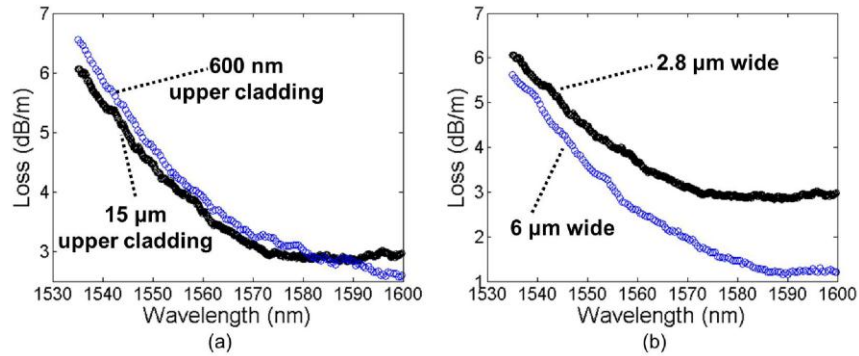

(a)   (b)

Fig. 6. (a) Measured TE propagation loss versus wavelength for 2.8 μm wide ULL waveguides with 600 nm (blue) and 15 μm (black) upper cladding thicknesses. (b) Measured TE propagation loss versus wavelength for 2.8 μm (black) and 6 μm (blue) wide cores.

4. Optical coupling between silicon and ULL waveguide layers

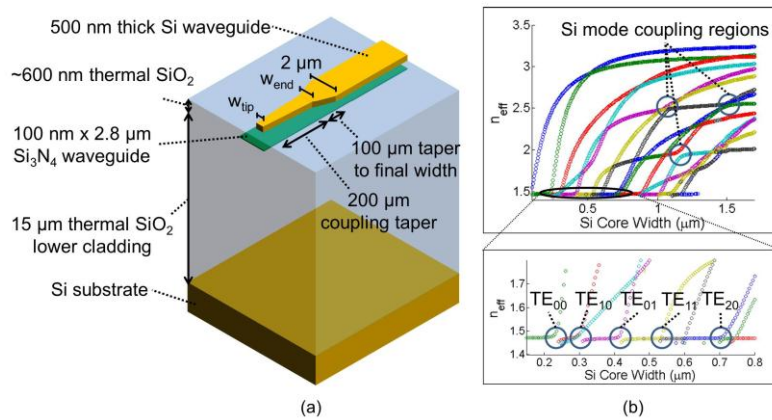### 4.1 Tapered waveguide couplers

(a)   (b)

Fig. 7. (a) Schematic of the structure used to couple light between ULL and Si waveguide layers, and (b) simulated effective indices for the two-waveguide structure versus Si waveguide width at 1550 nm (simulations are performed with Photon Design's FIMMWAVE software).

Figure 7(a) shows a schematic of the taper structure used for optical coupling between the ULL and Si waveguide layers. The Si waveguide is tapered laterally above the Si_3N_4 core having a fixed width of 2.8 µm. The structure is made up of two linearly tapered sections. The first 200-µm-long taper section couples a mode in the Si waveguide to the fundamental TE mode of the ULLW. Figure 7(b) shows how the effective mode indices of the asymmetric waveguide structure vary with the width of the Si waveguide's core. The bottom of Fig. 7(b) gives a closer look at this relationship near the effective index of the ULLW's fundamental TE mode (1.48). Circles indicate Si core widths at which the Si and ULL waveguides perturb each other such that coupling can occur. As shown in the figure, the fundamental TE mode of the ULLW can couple to the fundamental TE mode, as well as many higher order TE modes, of the Si waveguide depending on the values of w_{tip} and w_{end} shown in Fig. 7(a). In this work, we characterize coupling tapers with nominal w_{tip} values of 400 and 600 nm. In each case, w_{end} is 200 nm wider than w_{tip}.

Near Si core widths where the Si and the ULL waveguide modes are synchronous, an even supermode with significant power in each waveguide core is supported [14]. Figure 8 shows the effective indices of the structure versus Si core width near the crossing of the Si and ULL TE_{00} modes. The thin dashed lines show the effective indices of the Si and ULL waveguides alone (with no perturbation). The thinner blue and thicker green lines show the effective indices of the full two waveguide structure for t_{gap} values of 300 and 800 nm, respectively. The inset shows the vertical electric field distributions for various Si core widths in the structure having a t_{gap} of 800 nm. The operating principle of the taper can be understood as an adiabatic mode transformation between the ULL TE_{00} (inset 1a) and the Si TE_{00} (inset 3a) modes mediated by the even supermode of the structure (inset 2a). For a low loss taper design of this type, w_{tip} must be in a regime where the supermode index approaches the asymptote of the uncoupled ULLW mode (point 1a). Otherwise, the supermode has significant power in the Si waveguide that can be canceled out only through coupling to radiation modes at the taper tip. By increasing t_{gap} (decreasing the perturbation), a blunter taper tip may be used since the ULL waveguide's TE_{00} mode is further from cut-off and the even supermode's index approaches the asymptote more quickly with decreasing core width [15]. For the structure having a t_{gap} of 800 nm, one can also see that an even blunter low loss tip is possible because an odd supermode is supported for Si core widths narrower than the Si core's synchronous width (points 2a and 2b). This design would then function as a tapered directional coupler [16]. The coupling tapers in this work are designed as adiabatic mode transformers around $\lambda_0 = 1.55$ µm, though they may function as tapered directional couplers in some wavelength regimes.
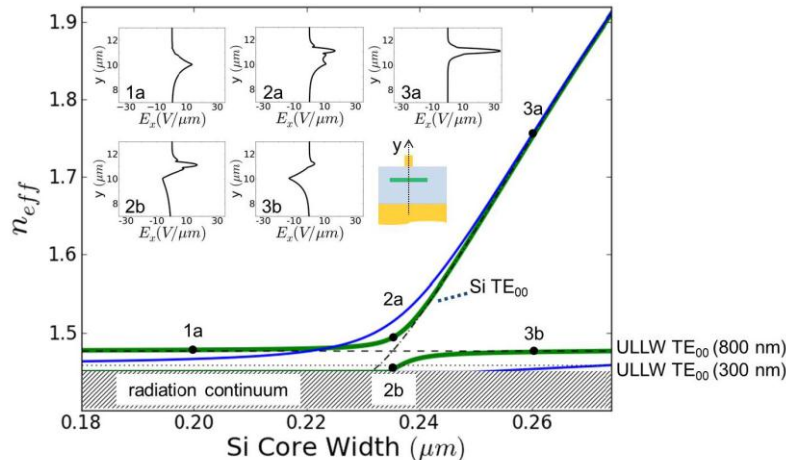

Fig. 8. Simulated effective indices versus Si core width. Simulations are performed with FIMMWAVE at $\lambda_0 = 1.55$ µm. The ULLW core thickness is 100 nm.

The second 100-μm-long taper section of the structure shown in Fig. 7(a) increases the confinement of the mode in the Si waveguide. The increased confinement enables tighter waveguide bends, and the higher-aspect-ratio core geometry decreases the sidewall scattering loss in the Si waveguide. For both structures in this work, the final Si waveguide width is 2 μm. Though the second taper was designed as a spot-size converter, the circles at the top of Fig. 7(b) indicate where this taper can also couple power between higher order TE and TM modes in the silicon waveguide. This effect is thoroughly investigated in [17], and transmission spectra discussed in Section 4.3 suggest that this mode conversion can limit the bandwidth of some structures with taper couplers.
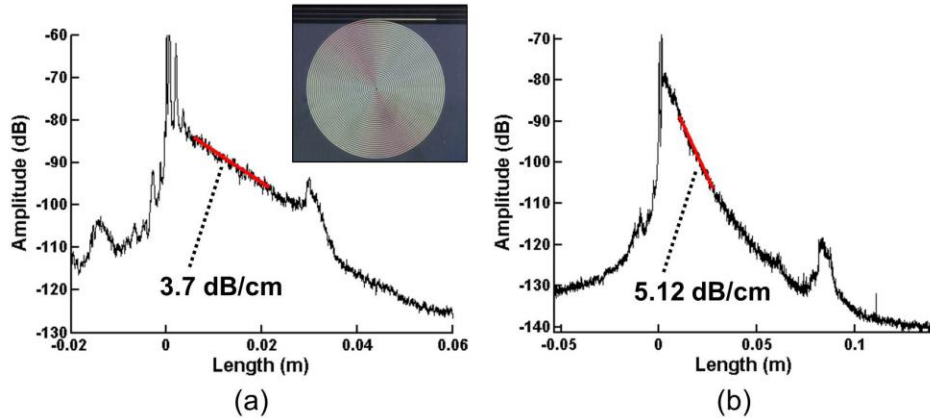
4.2 Si waveguide propagation loss

Fig. 9. Si waveguide backscatter data measured in spiraled waveguide after coupling tapers with (a) $w_{tip} = 400$ nm and (b) $w_{tip} = 700$ nm.

Figure 9 shows backscatter data measured in 78 mm long Si waveguide spiral-in structures like the one pictured in the Fig. 9(a). Light is coupled into the Si spiral from a single-mode ULL waveguide underneath. The spiral in Fig. 9(a) has a coupling taper with nominal dimensions $w_{tip} = 400$ nm and $w_{end} = 600$ nm, though scanning electron microscope images of the fabricated tapers indicate that the dimensions are ~150 nm wider than these nominal values. Simulations performed with Photon Design's FIMMPROP software indicate that this taper couples the fundamental TE mode of the ULL waveguide to the TE_{20} mode of the Si waveguide. Simulations also indicate that the taper to a 2 μm Si core width excites the TE_{01} and TM_{30} modes with significant power. Figure 9(a) shows a fit-calculated propagation loss of 3.7 dB/cm for the spiral. For spiral-in structures, waveguide backscatter increases with decreasing bend radius, and this is taken into account when fitting propagation loss [18]. At a distance of around 30 mm into the spiral, a large amount of the power radiates away. This radiation loss may be due to the lower core confinement of the TE_{01} mode, which radiates out whereas the other modes are still well confined.

Figure 9(b) shows data from a spiral with nominal coupling taper dimensions $w_{tip} = 700$ nm and $w_{end} = 900$ nm. In simulations of this design, the ULL waveguide couples to the TM_{50} mode of the Si waveguide. According to simulation, the second taper does not efficiently excite any other modes. The fit propagation loss of 5.12 dB/cm is higher than that obtained for the structure in Fig. 9(a). This may be due to the comparatively low sensitivity of the TE_{01} mode to sidewall roughness. The modal excitation for this design may also have higher confinement since the light propagates the full 78 mm of the spiral.

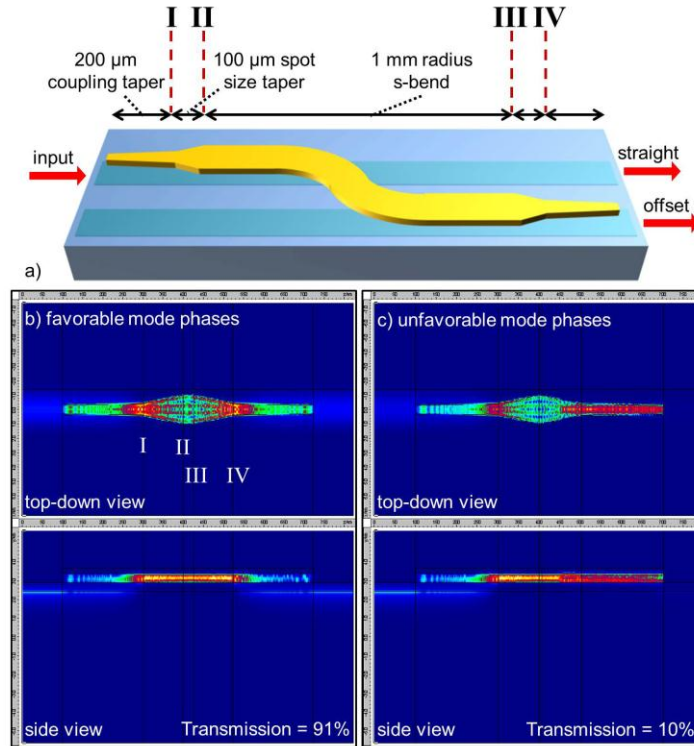*4.3 Transmission measurements of s-bend structures*

Fig. 10. (a) Schematic of the integrated s-bend structure used to characterize taper transition loss and bandwidth. Simulations at $\lambda_0 = 1.55$ μm show the average optical intensity in a multimode structure for cases of (b) favorable and (c) unfavorable mode phases at the output coupling tapers.

Figure 10(a) shows a schematic of the s-bend structure used to characterize the loss per transition between the ULL and silicon waveguide layers. Light is coupled into the input ULL waveguide using a 2-μm-spot-size tapered fiber. Light then couples up to the Si waveguide via the first 200 μm coupling taper. The modal confinement is increased in the 100 μm spot size taper before the light is offset with an s-bend having 1 mm bending radius. Finally, the light couples back down into an offset ULL waveguide using the same taper design. The s-bend structure is used to verify that the light is fully coupled to the silicon waveguide. To characterize this structure, transmission data is collected from "straight" and "offset" output ULL waveguides, as shown in the figure.

Before analyzing transmission data from s-bend structures, we first examine a multimoding effect that can limit their transmission bandwidth. As discussed in Section 4.1, the spot size taper may couple power between higher order modes of the Si waveguide in some cases. Figs. 10(b) and 10(c) show simulated average optical intensities for one such multimode taper structure performed with Photon Design's FIMMPROP software. The coupling taper couples the TE_{00} mode of the ULL waveguide to the TE_{20} mode of the silicon waveguide. The spot size taper then couples power to various higher order modes, such that significant power is in the TE_{20}, TE_{01}, and TM_{30} modes at interface *II*. Since the three modes travel with different phase velocities in the s-bend section, they arrive at interface *III* with relative phases that are different than those at interface *II*. Due to the mode coupling in the second spot size taper, the modal makeup (mode phases and amplitudes) of the field at interface *IV* is a function of the relative phases at interface *III*. This can result in the cancelation of field if two modes at interface *III* are converted to the same mode but with

offset phases in the spot size taper. Varying mode phases at interface *III* can also result in the strong excitation of a mode at interface *IV* that does not couple efficiently with the ULL waveguide underneath via the Si waveguide taper. According to simulation, the interference of modes with offset phases accounts for at most 2 dB of loss in the s-bend structure, while the mode-conversion effect can cause loss as great as 9 dB.

For the structure with "favorable mode phases" in Fig. 10(b), the relative phases of the modes at interface *III* are set by changing the length of waveguide between interfaces *II* and *III* such that the TE_{20} mode dominates at interface *IV*. The offset coupling taper is then nearly as efficient as the first, resulting in 91% transmission. For the structure with "unfavorable mode phases" in Fig. 10(c), the phases at interface *III* are such that the TE_{01} and TM_{30} modes are dominant at interface *IV*. The coupling taper is not designed to couple these modes to the TE_{00} mode of the ULL waveguide, and the transmission drops to 10%. So as the source wavelength is swept for a multimode structure, the relative phases of the modes change at interface *III*, resulting in a transmission oscillation with amplitude as high as 9.6 dB. This oscillation limits the transmission bandwidth of such a structure.
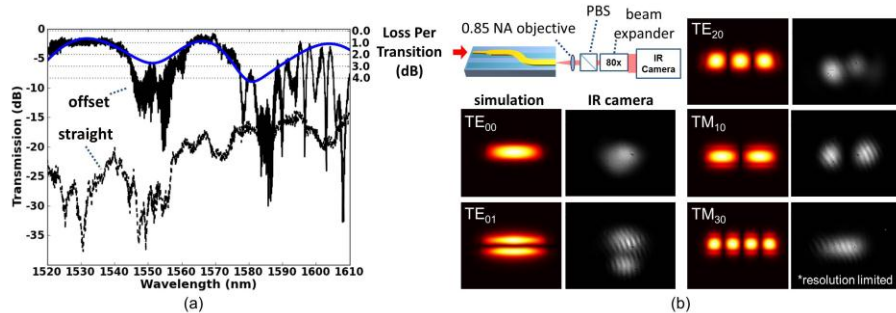

Fig. 11. (a) Transmission data through an integrated s-bend structure. The thick blue line shows the simulated transmission. (b) Simulated mode fields next to IR images of the modes obtained with a spatial and spectral technique near $\lambda_0 = 1.55$ μm. A schematic of the imaging setup is shown in the top left.

Figure 11(a) shows transmission data through an integrated s-bend structure with nominal coupling taper dimensions $w_{tip} = 400$ nm and $w_{end} = 600$ nm. Since the propagation loss in the Si waveguide was measured in Section 4.2 using the same modal excitation, it can be subtracted out of the transmission data to give the loss per taper transition as the right y-axis in Fig. 11(a). In the figure, one can see a minimum taper transition loss of (0.4 ± 0.2) dB in the 1565 nm wavelength regime for this structure. The transmission measured at the offset waveguide has a sinusoidal envelope with troughs near 1555 and 1585 nm, but corresponding peaks indicating uncoupled power are not observed in the straight waveguide data. This indicates that the troughs are likely due to a multimode structure, rather than a decrease of coupled power in the regime. A full simulation of the structure with FIMMPROP gives the transmission shown with a solid blue line over the data. The slow oscillations are due to the mode coupling in the spot size taper discussed above, and this effect limits the s-bend structure to a 3-dB bandwidth of 20 nm. The fast oscillations at larger wavelengths can be explained either by the excitation of a mode in the Si s-bend near cut-off (such that a larger phase difference builds up at interface III as the source wavelength is swept) or by a reflective cavity in the Si. If a single taper were used for coupling up to a terminal device in the Si, such as a photodiode, a larger bandwidth is expected.

Figure 11(b) shows the simulated mode fields in the silicon waveguide at interface *III* in the structure. Though the waveguide supports additional modes, the modes shown in the figure make up 99% of the total optical intensity at the interface according to the simulation. After transmission measurements, the s-bend structure was diced and polished at interface *III*, and a spatial-spectral (S^2) technique was used to extract mode images from the 2-μm-wide silicon waveguide there [15]. A polarizing beamsplitter cube separates the TE and TM mode

fields, and an $80 \times$ beam expander is used to fill the 256×320 pixel field of the infrared camera with the mode image. The modes imaged at interface *III* agree well with the simulation. However, the four intensity lobes of the TM_{30} mode are spaced below the resolution of the imaging system, and clear intensity nodes are not visible in the image.

Figure 12(a) shows transmission data through an integrated s-bend structure with nominal coupling taper dimensions w_{tip} = 700 nm and w_{end} = 900 nm. Again, the loss per taper transition is indicated by the right y-axis. From the figure, a minimum taper transition loss of (0.8 ± 0.2) dB is obtained. The slow sinusoidal envelope due to multimoding in the silicon waveguide is absent for this design, and the power measured at the straight waveguide output also increases where the power measured at the offset waveguide decreases. FIMMPROP simulations indicate that a single, TM_{50} mode dominates in the silicon waveguide of this structure. As a result, no modal interference or conversion takes place, and the structure has an increased 3-dB bandwidth of 100 nm.

The solid red line in Fig. 12(a) shows the loss per taper transition measured from an optical backscatter measurement. Loss values calculated from backscatter data agree well with those calculated from transmission measurements. Since the backscatter calculations do not depend on fiber-to-chip coupling losses, they confirm the (1.3 ± 0.2) dB per facet coupling loss value measured from transmission data. The loss taper transition loss is calculated by comparing the backscattered power, shown in Fig. 12(b), from three s-bend structures fabricated in series. The comparison is made in the spectral domain to yield the taper loss versus wavelength. From Fig. 12(b), one can also see the increase in waveguide backscatter in the tapered silicon waveguide sections, where light in the narrow core geometry is more sensitive to sidewall roughness scattering.
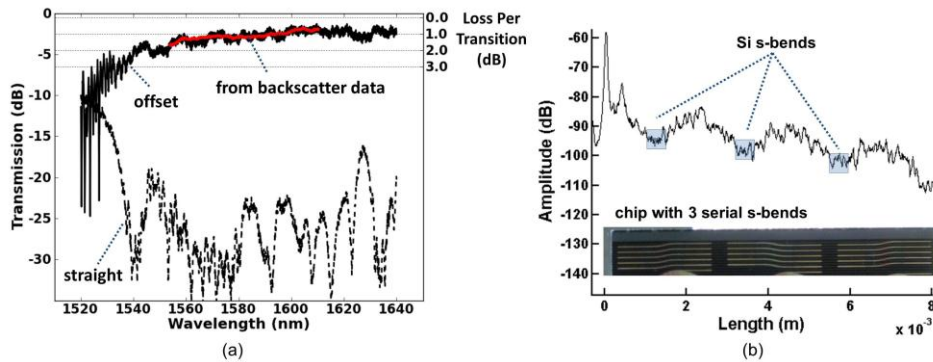

Fig. 12. (a) Transmission data through an integrated s-bend structure versus wavelength, and (b) backscatter data from a series of s-bend structures.

5. Discussion and conclusions

The tapered coupler designs presented in Section 4 are suitable for integrating ultra-low-loss waveguides with hybrid InP/Si active devices that can tolerate higher order modes in the Si waveguide. Since the taper tips are blunt, they can also be fabricated using lower resolution i-line photolithography. Though coupling is achieved with low loss and broad bandwidth, a typical hybrid InP/Si laser utilizes the fundamental TE_{00} mode in the silicon waveguide. Therefore, either a mode converter in the Si layer or direct coupling to the TE_{00} Si mode using narrower taper tips, around 220 nm as shown in Fig. 8, is necessary for the integration of a typical hybrid Si laser [6]. Furthermore, the planar waveguide resonators with the highest Qs use thinner, lower confinement Si_3N_4 cores. Simulations indicate that integration is possible with these waveguides using a thicker coupling gap layer of around 1 μm.

Acknowledgments